Experimental comparison of three methods to measure electron source properties for synchrotron radiation

N. Samadi,[1,*] X. Shi,[2,†] L. Dallin,[3] L. Assoufid,[2] and D. Chapman[4]

[1]*Department of Physics and Engineering Physics, University of Saskatchewan, 116 Science Place, Saskatoon, Saskatchewan S7N5E2, Canada*
[2]*Advanced Photon Source, Argonne National Laboratory, 9700 South Cass Avenue, Lemont, Illinois, 60439, USA*
[3]*Canadian Light Source, 44 Innovation Boulevard, Saskatoon, Saskatchewan S7N2V3, Canada*
[4]*Department of Anatomy, Physiology and Pharmacology, University of Saskatchewan, 107 Wiggins Road, Saskatoon, Saskatchewan S7N5E5, Canada*

(Received 4 February 2022; accepted 9 June 2022; published 30 June 2022)

Measuring the electron source size is essential for determining the emittance of synchrotron radiation. Pinhole imaging is the most common technique which measures the source profile in all transverse directions. The grating interferometry technique measures the coherence function of the x-ray beam, which indirectly determines the source size. The newly developed phase-space beam position and size monitor (ps-BPM) system provide information on electron source properties: position, angle, size, and divergence. These three techniques were used to determine the source size at a bend magnet beamline at the Canadian Light Source. In this work, we compare experimental results from these measurements at the same time, which is used as a cross-calibration procedure for each method.

DOI: 10.1103/PhysRevAccelBeams.25.062803

I. INTRODUCTION

Accurate measurements of source properties have gained increasing interest at current synchrotron light sources and even more so for next-generation low-emittance sources [1–3]. The knowledge of the size, divergence, position, and angle of the electron and x-ray source is critical for machine and beamline operation and experiment optimization. Existing source measurement techniques are mainly based on direct imaging and interferometry, with a newly added member based on the crystal energy-angle dispersion and the element K-edge [4,5]. We recently compared these three categories of radiation-based techniques by simulation [6], with each method showing advantages and limitations.

Pinhole imaging [7–9] is one of the most common direct-imaging techniques to measure the electron source profile and is widely used at current facilities. The system can provide source information in all transverse directions. However, the spatial resolution of pinhole imaging is limited by the point spread function of the pinhole and the detector resolution, making it challenging to measure source sizes below 10 μm [6].

Double-slit interferometry can be used to measure small source sizes but with a limited detectable size range for a fixed system [6]. Grating interferometry is another interference-based method primarily used for accurate wavefront measurements at synchrotron beamlines for source and optics characterization. It can also measure the transverse coherence function and, thus, the source size profile [10,11]. Unlike the double-slit method, grating interferometry is model-free and can provide more accurate measurements of the source size. However, the setup and measurement procedure is complicated and not widely used as a source diagnostic method.

We have developed a phase-space beam position and size monitor (ps-BPM) that can measure the electron source position, angle, size, and divergence at a single location and at the same time for a given transverse direction [4,5]. The system makes use of perfect crystal diffraction and the absorption K-edge of an element. The resolution of the method is driven by the signal-to-noise ratio. Simulation shows that sub 10 μm measurement is possible for fourth-generation synchrotron sources [6]. For accurate source size measurements, the knowledge of the K-edge width of the element is also essential but not always available. Therefore, the calibration of the instrument resolution function of the ps-BPM by other techniques is necessary.

In this work, we show the measurement of the electron source size at the Biomedical Imaging and Therapy (BMIT)

*Corresponding author.
nazanin.samadi@usask.ca
†Corresponding author.
xshi@anl.gov

Published by the American Physical Society under the terms of the Creative Commons Attribution 4.0 International license. Further distribution of this work must maintain attribution to the author(s) and the published article's title, journal citation, and DOI.

bend magnet beamline [12,13] at the Canadian Light Source (CLS), aiming to provide experimental insights into the three different types of methods compared under the same condition. The measurement geometry and cross-calibration procedure can be beneficial for the design and implementation of an integrated system at any future diagnostic beamline.

II. DESCRIPTION OF METHODS

A. Pinhole imaging

X-ray pinhole imaging was chosen for its popularity and straightforward setup. The system consists of a pinhole and an imaging detector at a source-to-pinhole distance p and pinhole-to-detector distance q, respectively. The optimization of a pinhole system for source size measurements was shown elsewhere [6]. Here we only summarize the main equations for the necessary data analysis.

For simplicity, the recorded image of the source is assumed to be a 2D Gaussian profile with the rms image size, $\sigma_{\mathrm{image},x,y}$, in the x and y directions given by

$$\sigma^2_{\mathrm{image},x,y} = \frac{q^2}{p^2}\sigma^2_{\mathrm{source},x,y} + \sigma^2_{\mathrm{pin}} + \sigma^2_{\mathrm{det}}, \tag{1}$$

where $\sigma_{\mathrm{source},x,y}$ is the source size, σ_{pin} and σ_{det} are the Gaussian rms sizes of the point spread function (PSF) of the circular pinhole and the detector, respectively. Once σ_{pin} and σ_{det} are determined, the source size can be extracted from Eq. (1) using the measured $\sigma_{\mathrm{image},x,y}$. Most of the existing pinhole imaging systems for source diagnostics are located at bend magnet (BM) beamlines. Since the photon source size of single-electron emission through a BM is negligible, $\sigma_{\mathrm{source},x,y}$ can be treated as the size of the electron source. Note that Eq. (1) is not limited to the x and y directions but applies to any transverse directions.

The σ_{pin} term in Eq. (1) can be obtained either analytically or through Gaussian fitting of the PSF from near-field simulation [6]. The latter was chosen for this work to have a better accuracy (see Sec. IV A for details). The optimized pinhole size can be determined from the expected source size by minimizing the $(p\sigma_{\mathrm{pin}})/(q\sigma_{\mathrm{source}})$ ratio [6]. For most source size cases, the optimized pinhole size is within the 20–30 μm range. In this study, we used a pinhole of 20 μm size because of availability.

The σ_{det} term can be measured with a sharp edge [8] or estimated analytically considering the diffraction and defect of focus [14]. In this work, σ_{det} is significantly smaller than the contributions of the other two terms in Eq. (1), thus only the analytical method was used.

B. Grating interferometry

Grating interferometry is an interference-based technique, an advanced version of double-slit interferometry. The main principle of interference-based methods is based on the van Cittert-Zernike theorem, which states that the spatial coherence function is the Fourier transform of the source distribution function. For a Gaussian BM source, the transverse coherence function of the x-ray beam at a distance L downstream of the source is also a Gaussian function. By measuring the rms size of the Gaussian coherence function, namely the coherence length $\xi_{x,y}$, the source size can be obtained as [15]

$$\sigma_{\mathrm{source},x,y} = \frac{\lambda L}{2\pi\xi_{x,y}}, \tag{2}$$

where λ is the x-ray wavelength.

Grating interferometry uses the visibility (contrast) of recorded interferograms downstream of a transmission grating to measure the coherence function of the beam. Linear [16], 2D checkerboard [10,17], and circular [11] gratings have been used to extract coherence lengths in single and multiple transverse directions. Since grating measurements give the integrated coherence information over the measured beam area, when using linear or 2D checkerboard gratings, only the projected source size $\Sigma_{\mathrm{source},x,y}$ along the diffraction directions of the grating can be obtained. When a circular grating is used, source size along any transverse direction can be extracted. In this work, we used the 2D checkerboard grating to focus on the measurements along the horizontal and vertical directions.

The setup contains a grating at a source-to-grating distance L and a detector at a variable grating-to-detector distance z. The visibility of the interferograms as a function of z is given by [18]

$$V_{x,y}(z) = A_{x,y}\left|\sin\left[\frac{\pi\lambda z L}{p^2_{x,y}(L+z)}\right]\right|\exp\left[\frac{-2\pi^2 z^2\Sigma^2_{\mathrm{source},x,y}}{p^2_{x,y}(L+z)^2}\right], \tag{3}$$

where $A_{x,y}$ is the scaling parameter and $p_{x,y}$ is the period of the interference pattern of the grating in x and y directions. For a checkerboard π-phase grating with a period of p_0 aligned along the edge direction of the square pattern, we have $p_x = p_y = p_0/2$. Note that a π-phase grating means that the phase shifts of the transmitted x ray generated by the alternating blocks are different by π, or a pathlength difference of $\lambda/2$.

The sine oscillation term in Eq. (3) represents the repeating appearance of the Talbot self-imaging [19] of the pattern with the period $p_{x,y}$. In other words, the visibility of the interferogram peaks at the Talbot distances where the sine term is unity. The exponential term is the Gaussian coherence function of the beam. By fitting the measured visibility function, the projected source size $\Sigma_{\mathrm{source},x,y}$ can be extracted. We should note that

grating interferometry is, in principle, model-free, which means no prior assumption of the shape of the coherence function is necessary. However, we assumed a Gaussian shape to be consistent and comparable with the other two methods. Furthermore, the scaling parameter $A_{x,y}$ in Eq. (3) accounts for the spatial resolution of the entire system including the PSF of the detector and other static background noise. The source size is extracted from the relative decay rate of the visibility, which is not sensitive to the absolute value of the visibility. Therefore, the exact value of the detection system resolution is not needed to extract the source size as long as the detector can resolve the interferogram pattern with enough contrast (visible harmonic peaks in the Fourier-transform images, see Sec. IV B for details).

C. ps-BPM

A phase-space beam position and size monitoring system (ps-BPM) has been developed at the Canadian Light Source (CLS), which can measure the position, angle, size, and divergence of the electron source of a synchrotron at a single location and at the same time in a given direction [4,5]. The system includes a crystal monochromator that tunes the photon energy to the K-edge of a selected filter, a K-edge filter, and a detector.

Thanks to the dispersive properties of the silicon monochromators, the photon beam will have an energy dispersion in the vertical plane (diffraction plane) around the central energy of the K-edge filter. When the K-edge filter is placed in the beam (edge side), the width of the K-edge, σ_{edge}, measured by a detector placed at a distance D from the source, contains the projected electron source size, $\Sigma_{\mathrm{source},y}$, the natural energy width of the K-edge, $\sigma_{y'_{\mathrm{K-edge}}}$ and the angular bandwidth of the monochromator crystal, $\sigma_{y'_{\mathrm{mono}}}$. For Gaussian shape functions, the electron source size can be obtained by

$$\Sigma_{\mathrm{source},y} = \sqrt{\sigma_{\mathrm{edge}}^2 - \sigma_{\mathrm{IRF}}^2}, \tag{4}$$

where σ_{IRF} is the width of the instrument resolution function (IRF) and can be calculated as

$$\sigma_{\mathrm{IRF}} = \sqrt{(D\sigma_{y'_{\mathrm{K\text{-}edge}}})^2 + (D\sigma_{y'_{\mathrm{mono}}})^2}. \tag{5}$$

The photon beam without the K-edge filter (beam side) imaged by the detector will include the projected electron source size, $\Sigma_{\mathrm{source},y}$, the projected electron source divergence, $\Sigma_{\mathrm{source},y'}$, and the natural opening angle of the photon beam, $\sigma_{y'_{\mathrm{Ph}}}$. From that, one can calculate the electron source divergence by

$$\Sigma_{\mathrm{source},y'} = \frac{1}{D}\sqrt{\sigma_{\mathrm{beam}}^2 - \Sigma_{\mathrm{source},y}^2 - (D\sigma_{y'_{\mathrm{Ph}}})^2}. \tag{6}$$

The ps-BPM takes advantage of the large horizontal width of the bend magnet radiation, where half of the beam is covered with the K-edge filter and the other half is just the monochromatized direct beam. These two pieces are then detected by an imaging camera enabling measuring the source size and divergence simultaneously. This information is obtained by the widths of the detected beam side and K-edge width on the edge side. At the same time, the center location of the edge and beam side will give information about the source position and angle.

III. EXPERIMENTAL SETUP AND DATA ACQUISITION

The experiment was performed at the BMIT-BM beamline at the CLS. A schematic of the experimental setup combining all three measurement techniques is shown in Fig. 1. A Si (2,2,0) double-crystal monochromator (DCM) located at 12.5 m from the BM source was used to tune to the desired x-ray photon energy. The imaging hutch at the BMIT-BM consisted of two optical tables allowing for our experiments with multiple setups and detectors happening at the same time. The pinhole, barium K-edge filter, and a flat panel area detector were on the upstream optical table; the grating setup with a high-resolution detector was on the downstream optical table. Each component was mounted on translational stages allowing us to move them in and out of the beam.

Since the pinhole and grating measurements used the same detector, one was moved out of the field of view when the imaging was done using the other one. The ps-BPM was using a small part of the horizontal fan of the beam, and the setup was always in the beam, making measurements simultaneously with each of the other two methods.

The pinhole imaging measurements were done at multiple energies, including 18.0, 20.0, and 37.4 keV photon energies with a 20 μm diameter pinhole made of 95% Pt and 5% Ir with a graded thickness profile. The pinhole to the source distance, p, was 20.0 m, and the pinhole to the detector distance, q, was 5.0 m. The images were recorded by a hi-res detector system, a combination of a 100 μm thick LuAG:Ce scintillator, a 10x objective lens, and an Andor Neo sCMOS camera with a pixel size of 6.5 μm. This resulted in a 0.65 μm effective pixel size. The spatial resolution of this hi-res detector, σ_{det}, is estimated to be 2.2 μm based on the formula in the literature [14].

For the grating interferometry measurements, a checkerboard π-phase grating with a period of $p_0 = 4.8$ μm ($p_x = p_y = 2.4$ μm) was used with a grating to the source distance, $L = 24.5$ m. The grating-to-detector distance, z, is varied from 10 to 460 mm in 5 mm steps. At each grating-to-detector step, an image was recorded with the same hi-res detector at the same 20 keV photon energy. The exposure time of each image was 60 s.

The ps-BPM measurements were done around the barium K-edge at 37.441 keV, where half of the beam

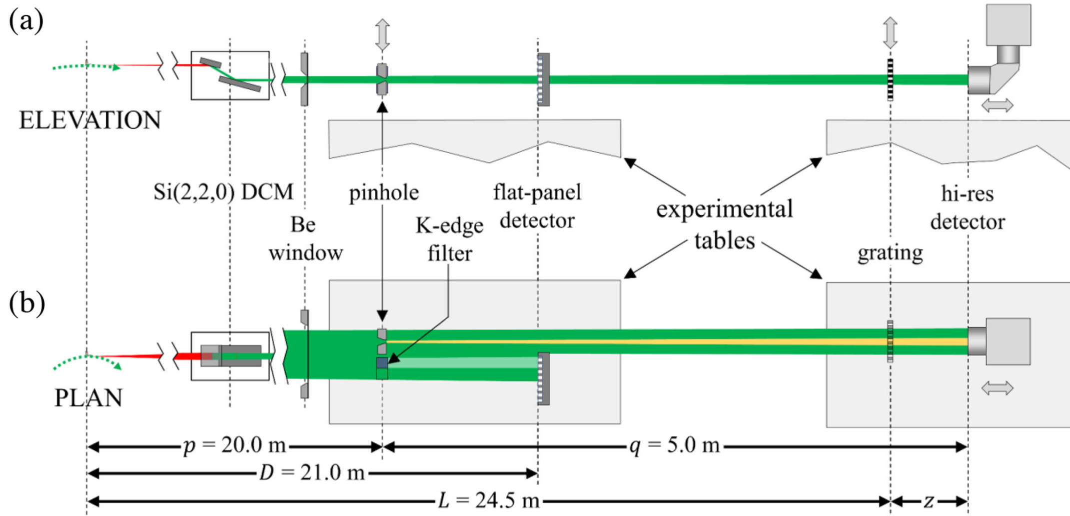

FIG. 1. Schematic of the experimental setup at BMIT-BM beamline for measuring the source size with three different techniques: pinhole imaging, grating interferometry, and K-edge-based ps-BPM.

was covered with a 35 $\mathrm{mg/cm^2}$ barium chloride solution filter (edge side) and the other half was just the mono beam with no K-edge filter (beam side). These two sides of the beam were then imaged simultaneously by a flat panel Hamamatsu (Hamamatsu Photonics, Hamamatsu City, Shizuoka Pref., Japan) detector with a pixel size of $100\ \mu\mathrm{m} \times 100\ \mu\mathrm{m}$ and a frame rate of 33 Hz. The barium filter was 20 m from the source and the detector-to-source distance, D, was 21 m.

IV. DATA ANALYSIS AND RESULTS

A. Pinhole imaging

The pinhole image recorded at 20 keV is shown in Fig. 2. The DCM was detuned to remove the effects of x rays at high-harmonic energies (e.g., mainly the 40-keV beam from the Si (4,4,0) diffraction). The beam profile shown in Fig. 2 is the sum of two images with 300 s acquisition, each using the hi-res detector.

The rms image size $\sigma_{\mathrm{image},x,y}$ was extracted through a 2D Gaussian fitting of the recorded image profile

$$I(x,y) = I_0 \exp\left[-\left(\frac{\cos^2\alpha}{2\sigma^2_{\mathrm{image},x}} + \frac{\sin^2\alpha}{2\sigma^2_{\mathrm{image},y}}\right)x^2 - \left(\frac{\sin 2\alpha}{4\sigma^2_{\mathrm{image},x}} - \frac{\sin 2\alpha}{4\sigma^2_{\mathrm{image},y}}\right)xy - \left(\frac{\sin^2\alpha}{2\sigma^2_{\mathrm{image},x}} + \frac{\cos^2\alpha}{2\sigma^2_{\mathrm{image},y}}\right)y^2\right], \quad (7)$$

where I_0 is the intensity fitting parameter, and α is the angle between the main axis of the fitted 2D Gaussian and the horizontal direction, as indicated in Fig. 2. The integrated image profiles in the horizontal and vertical directions are shown as solid lines in the top and right panels in Fig. 2, respectively. The rms size of the 1D Gaussian fitting (dashed curves in the top and right panels in Fig. 2) to the integrated profiles is the projected image size $\Sigma_{\mathrm{image},x,y}$, which can be used to extract the projected source size $\Sigma_{\mathrm{source},x,y}$ using Eq. (1) as well.

To extract the source sizes using Eq. (1), σ_{pin} needs to be computed accurately. The pinhole PSF was calculated by near-field (Fresnel) simulation taking into account the

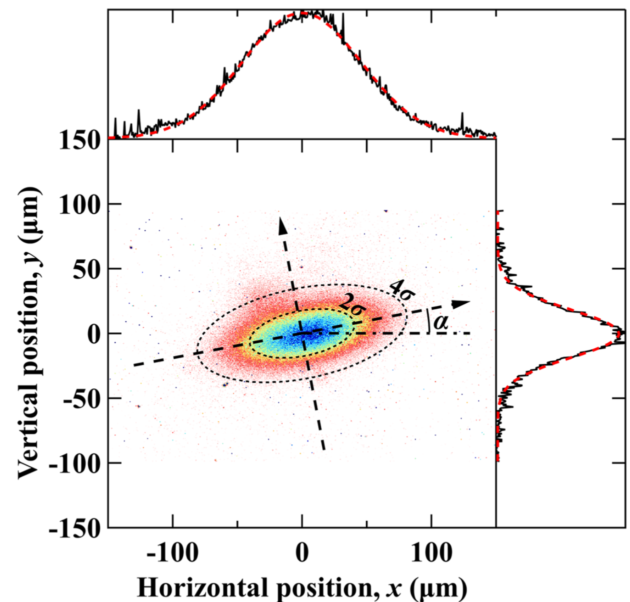

FIG. 2. The pinhole image of the source on the hi-res detector (left-bottom panel). The dotted curves represent the 2σ and 4σ contour lines of the fitted 2D Gaussian profile along the dashed axes. The integrated intensity profiles (solid curves) and the Gaussian fitting (dashed curves) in the horizontal and vertical directions are shown in the top and right panels, respectively.

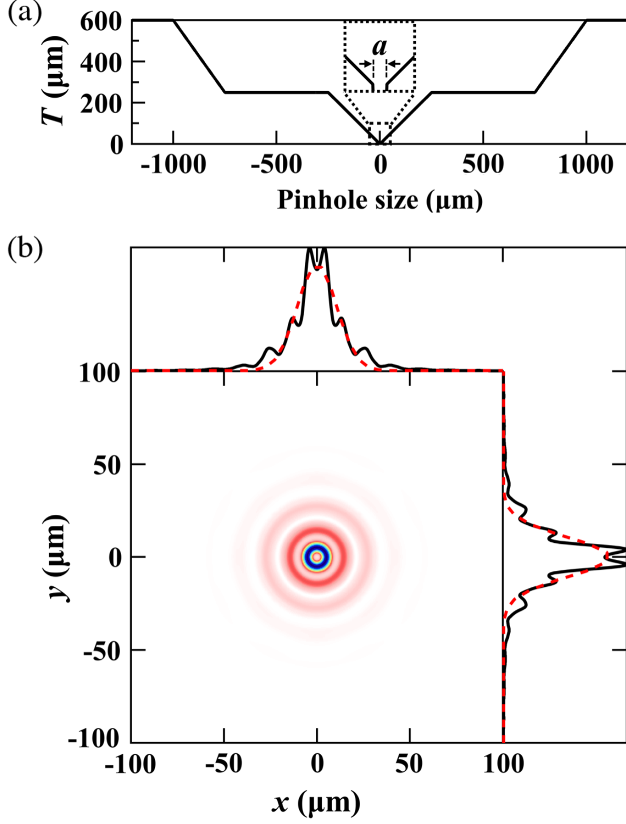

FIG. 3. (a) Thickness profile of the pinhole cross section. (b) Simulated pinhole PSF at 20 keV (left-bottom panel) and the integrated PSF functions (solid curves) along the x (top panel) and y (right panel) directions, respectively, with the Gaussian fitting shown as dashed curves. The pinhole diameter is 20 μm. The 2D Gaussian fit gives $\sigma_{\text{pin}} = 8.4$ μm. The 1D Gaussian fit of the integrated PSF gives the projected values of $\Sigma_{\text{pin}} = 11$ μm.

pinhole transmission function. The pinhole used has a circular symmetry with the thickness profile of the cross section shown in Fig. 3(a). The x-ray wavefield impinged on the pinhole is assumed as a spherical wave emitted from the BM source position, or

$$\varepsilon_0(x_0, y_0) = \frac{p}{\sqrt{p^2 + x_0^2 + y_0^2}} \exp\left\{ i\frac{2\pi}{\lambda}\left[\sqrt{p^2 + x_0^2 + y_0^2} - p\right] \right\}, \quad (8)$$

in the pinhole plane coordinate (x_0, y_0). Under the thin-optics approximation, the wavefield $\varepsilon_1(x_1, y_1)$ after the pinhole is then modulated by the pinhole thickness profile $T(x_0, y_0)$, given by

$$\varepsilon_1(x_1, y_1) = \varepsilon_0(x_0, y_0) \exp\left[-\left(\frac{\mu}{2} + i\frac{2\pi\delta}{\lambda} \right) T(x_0, y_0) \right], \quad (9)$$

where μ and δ are the linear attenuation coefficient and the refractive index decrement of the pinhole material, respectively. The wavefield on the hi-res detector plane can be simulated by the free-space propagation using

$$\varepsilon(x, y) = \frac{1}{i\lambda q} \iint_{-\infty}^{\infty} \varepsilon_1(x_1, y_1) \times \exp\left\{ \frac{i\pi}{\lambda q}\left[(x - x_1)^2 + (y - y_1)^2\right] \right\} dx_1 dy_1. \quad (10)$$

And the pinhole intensity PSF is then

$$I_{\text{pin}}(x, y) = \varepsilon(x, y) \cdot \varepsilon^*(x, y). \quad (11)$$

Figure 3(b) shows the simulated pinhole PSF at 20 keV showing clear diffraction fringes due to the near-field diffraction of the pinhole. Note that the pinhole used was not a high aspect ratio pinhole. Therefore, the PSF was simulated with the 2D pinhole thickness profiles [Fig. 3(a)]. The rms size of the pinhole PSF is then obtained by a 2D Gaussian fitting. Similarly, the projected PSF size is approximated by 1D Gaussian fitting (dashed curves) of the integrated PSF (solid curves), as shown in the top and right panels of Fig. 3(b).

Using the simulated σ_{pin} and $\sigma_{\text{det}} = 2.2$ μm, the source size can be extracted using Eq. (1) with the pinhole image size obtained from Eq. (7). The extracted source sizes at different photon energies are summarized in Table I. In cases when high energy photons (e.g., the first-harmonic energy at 37.4 keV or the second-harmonic energy component (40 keV) when DCM is tuned to 20 keV) exist, the extracted source size values are significantly larger than in the other cases. The main reason is the significant scattering background caused by the partial transmission of the pinhole at these high energies. Since we could not find a proper pinhole designed for high energies during the experiment, we tried to remove the higher energy components instead. When the DCM was detuned at 20.0 keV, the second-harmonic energy components at 40 keV were eliminated, resulting in much smaller extracted source sizes than in the turned case, as shown in Table I. This directly indicates that the high energy component (40 keV)

TABLE I. Extracted source sizes and tilt angles from pinhole imaging measurements at different energies.

Energy (keV) [K-edge]	DCM detune	$\sigma_{\text{source},x}$ (μm)	$\sigma_{\text{source},y}$ (μm)	α (°)
37.4 [Ba]	No	189 ± 2	120 ± 1	11.8 ± 0.5
20.0 [Mo]	No	186 ± 2	104 ± 2	12.4 ± 0.8
20.0 [Mo]	Yes	160 ± 3	60 ± 3	11.4 ± 0.5
18.0 [Zr]	Yes	158 ± 1	61 ± 1	11.7 ± 0.2
XSR pinhole	…	186[a] (165[b])	61[a] (60[b])	7.5

[a]Source size values directly measured at the XSR BM location.
[b]Scaled BMIT source size values based on XSR pinhole results and machine parameters.

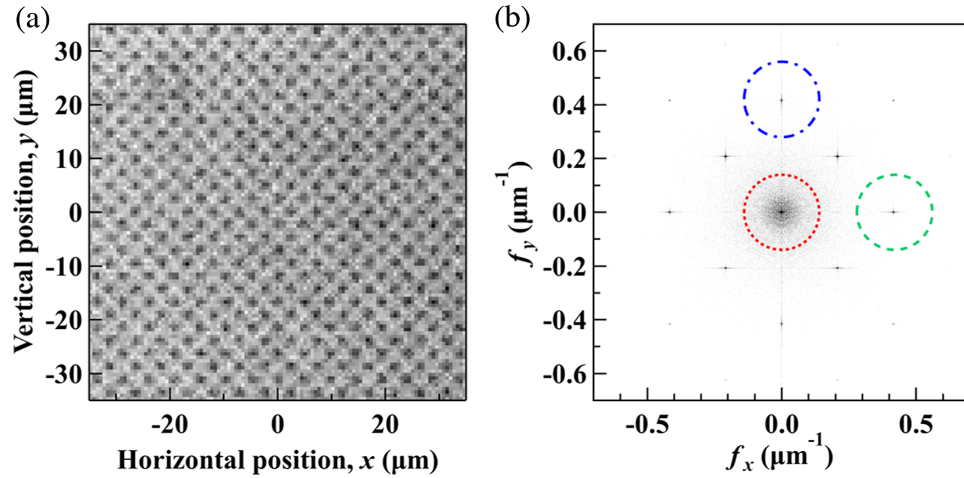

FIG. 4. Measured interferogram (a) and its Fourier-transform image (b) of a π-phase grating at the first Talbot distance.

had a significant transmission through the current pinhole and caused data analysis issues. Table I also included source size values recorded at the diagnostic BM beamline, x-ray synchrotron radiation (XSR) [20] using a visible-light pinhole camera. Since XSR and BMIT are at different lattice locations, we cannot directly compare the source values. Instead, the scaled BMIT source size values using XSR pinhole results and machine parameters are included in Table I, showing reasonable agreement with the BMIT pinhole results at 20.0 and 18.0 keV with detuned DCM. Based on the nominal design of the lattice, we know that the vertical source sizes of the two beamlines are close, which is also confirmed by Table I. The agreement between BMIT and XSR results suggests that the major optical effects (DCM higher harmonics and pinhole partial transmission) are successfully removed from the data acquisition by detuning the monochromator.

B. Grating interferometry

The interferogram of the grating at a grating-to-detector distance of $z = 45$ mm, corresponding to the first Talbot distance, is shown in Fig. 4(a) as an example. The checkerboard π phase grating gives a signature mesh pattern with a pattern period of 2.4 μm, half of the grating period. The visibility of the periodic pattern can be obtained by a Fourier-transform-based analysis [10]. The Fourier-transform image of Fig. 4(a) is shown in Fig. 4(b), where the central peak (within the dotted circle) represents the average intensity of the interferogram while the other harmonic peaks contain the information on the average contrast of different spatial frequencies. For example, the first harmonic peaks within the dashed and dash-dotted circles in Fig. 4(b) represent the contrasts of the 2.4 μm ($f_x = f_y = 0.417\ \mu\mathrm{m}^{-1}$) periodicity in the x and y directions, respectively. The visibility (V_x and V_y) of the pattern is then defined as the magnitude ratio between the harmonic peak and the central peak.

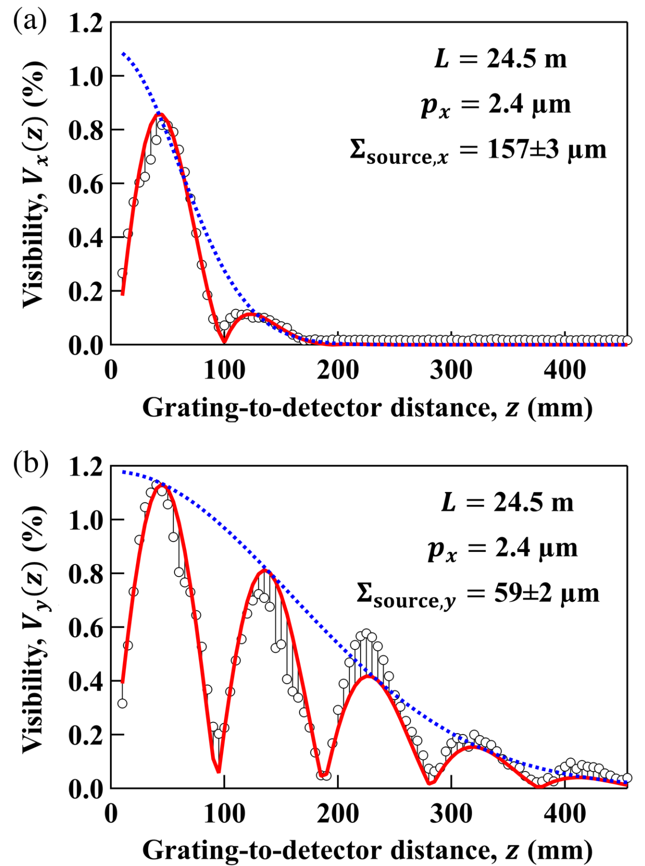

FIG. 5. Measured interferogram visibility (circles) as a function of the grating-to-detector distance in the horizontal (a) and vertical (b) directions. The solid curves are the fitted visibility curve using Eq. (3) with the listed parameters. The dotted curves are the fitted Gaussian coherence function [i.e., the exponential term in Eq. (3)], which forms the envelope function of the visibility curves. Note that in (b), the second peak is lower, and the third peak is higher than the fitting, which contributes mainly to the fitting error. This was due to the slight deviation (2%) of the grating duty cycle as confirmed by simulation previously [10].

TABLE II. Projected source sizes extracted from grating interferometry and pinhole imaging measurements at 20 keV at the BMIT-BM beamline.

Technique	$\Sigma_{\mathrm{source},x}$ (μm)	$\Sigma_{\mathrm{source},y}$ (μm)
Grating interferometry	157 ± 3	59 ± 2
Pinhole imaging	155 ± 3	61 ± 2

The extracted visibilities are then plotted as a function of grating-to-detector distance, as shown in Fig. 5 in both transverse directions. The projected source sizes are obtained by fitting the visibility curves to Eq. (3) and summarized in Table II. The results from pinhole imaging and grating interferometry show good agreements. Both measurements were carried out at the same photon energy

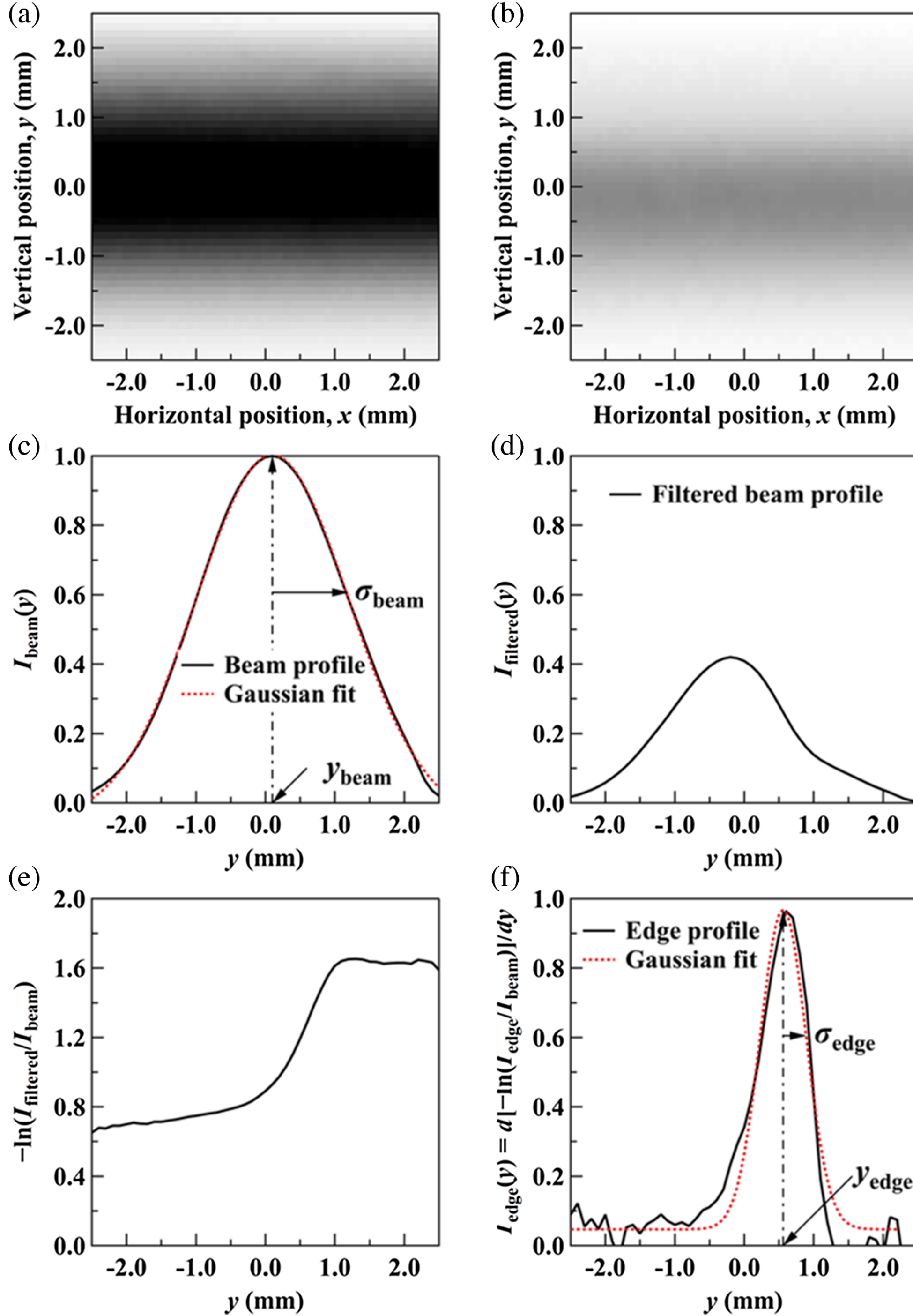

FIG. 6. Images of the beam (a) without the K-edge filter (beam side) and (b) with the K-edge filter (edge side). (c) Horizontally averaged beam profile, $I_{\mathrm{beam}}(y)$, and a Gaussian fit. (d) Horizontally averaged filtered beam profile, $I_{\mathrm{filtered}}(y)$. (e) The negative logarithm of the normalized $I_{\mathrm{filtered}}/I_{\mathrm{beam}}$ profile, and (f) its derivative with Gaussian fit.

(20 keV). Note that the projected horizontal sizes $\Sigma_{\mathrm{source},x}$ for the pinhole measurement in Table II are smaller than the $\sigma_{\mathrm{source},x}$ values in Table I, which is because of the source tilting angle. The measured tilting angle in Table I may also contain the systematic alignment error (<1°) between the detector reference surface and the horizontal plane. However, since we used the same detector setup for both the pinhole and grating measurements, the relative comparison between the two methods is still valid.

The grating interferometry measurements can provide accurate source sizes but with very low efficiency. The overall measurement time for each visibility data set was nearly 2 h, with a 60-s acquisition time for each image. The x-ray pinhole imaging measurement was faster but required minutes of exposure due to the low flux through the small pinhole, such as 300 s for 20 keV with detuned DCM.

C. ps-BPM

The ps-BPM measurements were faster because of its single-shot feature and high flux using the entire vertical BM fan. The calibration of the ps-BPM system was carried out by matching the projected source size to that of the pinhole and grating measurements (we chose the average value of the two measurements, or $\Sigma_{\mathrm{source},y} = 60\ \mu$m). Since the source size at a bending magnet beamline is dominated by electrons and is thus independent of photon energy, the results from pinhole and grating measurements at 20 keV can be used to extract IRF of ps-BPM using Eq. (4) at 37.4 keV or any other energies. The ps-BPM system can only measure the source size in the vertical direction, which is the diffraction plane of the DCM.

Figure 6(a) gives an example image of the photon beam without the K-edge filter (beam side), and Fig. 6(b) shows the K-edge filtered side of the data (edge side) imaged on the detector. Both sides of the beam are corrected for the dark response of the detector and horizontally averaged along x direction to obtain beam profiles, $I_{\mathrm{beam}}(y)$ and $I_{\mathrm{filtered}}(y)$, in Figs. 6(c) and 6(d), respectively. $I_{\mathrm{beam}}(y)$ is then fitted to a Gaussian function from which σ_{beam} is extracted. The negative logarithm of the normalized $I_{\mathrm{filtered}}/I_{\mathrm{beam}}$ profile is shown in Fig. 6(e), of which the derivative function can be fit to a Gaussian profile to determine the edge width σ_{edge}, as shown in Fig. 6(f) [5].

Using the data analysis process described above in Fig. 6, we obtained the average edge width, $\sigma_{\mathrm{edge}} = 331.1\ \mu$m over a total of 90-s acquisition. To match the average pinhole and grating result of $\Sigma_{\mathrm{source},y} = 60\ \mu$m, the IRF term in Eq. (4) needs to be $\sigma_{\mathrm{IRF}} = 327.7\ \mu$m. Note that this value is larger than the theoretical value ($\sigma_{\mathrm{IRF}} = 275\ \mu$m using Eq. (5) with $\sigma_{y'_{\mathrm{K-edge}}} = 13.0\ \mu$rad, $\sigma_{y'_{\mathrm{mono}}} = 2.2\ \mu$rad, and $D = 21$ m) given in [21] based on the reported pure-element Ba K-edge width in [22] and the Darwin width of Si (220) diffraction at 37.4 keV. The deviation arises from the broadening of K-edge width due to the elements in the barium compound, the chemical environment of the filter solution, and the Gaussian approximation in our model. We should also note that the IRF can be used for all measurements for a ps-BPM system, i.e., the system is calibrated.

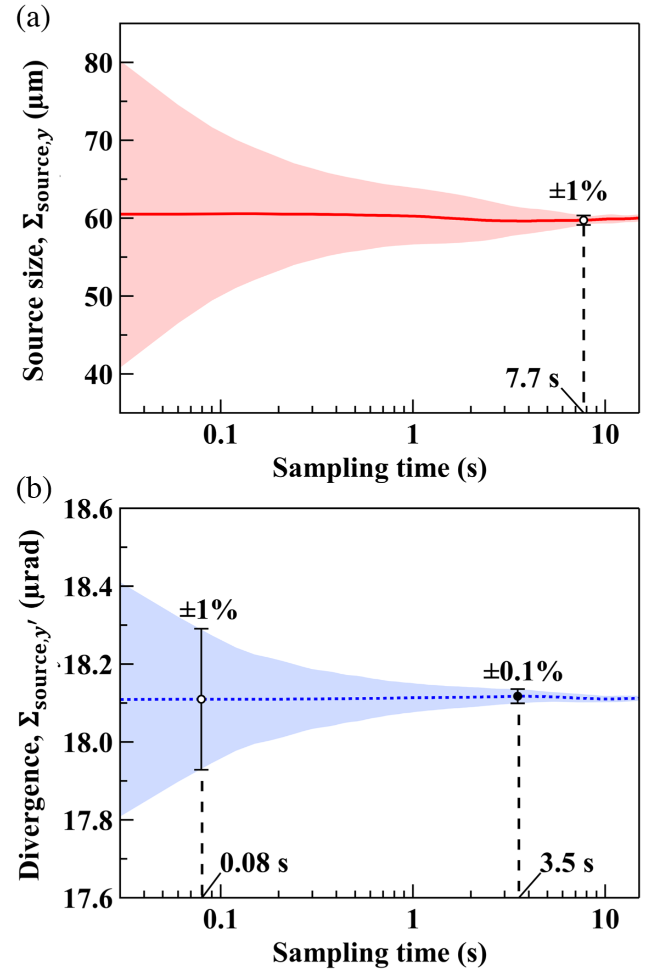

FIG. 7. Measured source size (a) and divergence (b) as a function of sampling time using the ps-BPM system. The colored shade shows the plus-minus standard deviation (STD) of 100 measurements. Dashed lines and markers indicate sampling time to achieve different measurement sensitivities.

The extracted source size as a function of sampling time is shown in Fig. 7(a). The colored shade shows the plus-minus standard deviation (STD) of 100 measurements with different sampling times. To achieve a sensitivity better than 1% STD, the acquisition time needs to be larger than 7.7 s.

The ps-BPM system also gives the divergence of the source [Fig. 7(b)] extracted from Eq. (6) with the calculated photon divergence term $\sigma_{y'_{\mathrm{Ph}}} = 48.1\ \mu$rad [5]. The sensitivity of the system is better than 1% at a 10 Hz measurement rate.

V. CONCLUSION

Three radiation-based techniques were used to measure the electron source size at the same beamline. We showed the comparison and cross-calibration between these methods.

The x-ray pinhole imaging technique can provide a real 2D image of the source, including the information on the source tilting angle, which cannot be obtained from the other two methods. The accurate modeling of the pinhole PSF is essential but difficult to account for all contributions, for example, penetration of high-harmonic-energy photons. The low-flux problem for the monochromatic x-ray pinhole imaging makes it sensitive to scattering and limits its real-time application. Broadband (white or pink beam) pinhole imaging will be necessary for fast measurements. The resolution of the system relies on the accurate modeling of the pinhole PSF, taking into account the broad bandwidth and pinhole transmission.

The grating interferometry is an accurate model-free method and can measure very small source sizes by choosing a small grating period (consequently high-resolution detector) and large detector distances [23]. For example, a 5 μm source size can be measured with a grating period of 2 μm and a 2 m detector scan distance. The method requires multi-images recorded at different detector positions, which is not suitable for real-time measurements. Its main application is to serve as a calibration reference and study complicated coherence problems.

The ps-BPM system was already validated as a powerful real-time source position and angle monitor. We showed that once calibrated, it can also be a useful source size and divergence monitor. The sensitivity of the system is dominated by the signal-to-noise ratio, which requires careful system design with proper scattering noise reduction. The system is normally used for source measurement in the vertical direction at a bend magnet beamline.

All three methods were carried out under similar conditions, including the DCM. The cross-calibration process is thus independent of the DCM-generated beam distortion, for example, by the thermal loading and mechanical vibration. If it exists, the thermal bump on the DCM will introduce a broadening of the virtual source size at the BM center, which is similar for all three methods. The contribution of the DCM vibration can also broaden the virtual source size, which can be further identified by time-frequency analysis [24]. Since the acquisition time for the three methods is longer than a few seconds, mechanical vibration effects (typically faster than a few Hz) can also be treated as a static virtual source size broadening.

Finally, the combination of different diagnostic tools still requires further studies, especially for next-generation light sources [6]. For example, the ps-BPM system has better performance at higher photon energies above 30 keV, where high-aspect-ratio pinholes (or double slits and gratings) are extremely hard to manufacture. The whitebeam pinhole imaging remains a good option for fast 2D source size diagnostics but with difficulties for source sizes below 10 μm. Alternative to grating interferometry, the double-slit interferometry can be used in either direction and can provide accurate source size measurement and calibration for pinhole imaging and the ps-BPM system. Nevertheless, the presented work is the first attempt to cross-compare methods from all three different categories, which is especially important for the relatively new ps-BPM method. The data analysis and cross-calibration process can help guide the future design and operation of diagnostic beamlines.

ACKNOWLEDGMENTS

The authors acknowledge the financial support of the Natural Sciences and Engineering Research Council of Canada (NSERC) Discovery Grant, the Saskatchewan Innovation and Opportunity Scholarship, the Government of Saskatchewan, and the University of Saskatchewan. The research described in this paper was performed at the Canadian Light Source, which is funded by the Canada Foundation for Innovation, NSERC, the National Research Council Canada, Canadian Institutes of Health Research, the Government of Saskatchewan, Western Economic Diversification Canada, and the University of Saskatchewan. This work was also supported by the U.S. Department of Energy, Office of Basic Energy Sciences, under Contract No. DE-AC02-06CH11357.

[1] M. Eriksson, J. F. Van Der Veen, and C. Quitmann, Diffraction-limited storage rings–A window to the science of tomorrow, J. Synchrotron Radiat. **21**, 837 (2014).

[2] P. F. Tavares, S. C. Leemann, M. Sjöström, and Å. Andersson, The MAX IV Storage Ring Project, J. Synchrotron Radiat. **21**, 862 (2014).

[3] M. Borland *et al.*, The upgrade of the advanced photon source, in *Proceedings of the 9th International Particle Accelerator Conference (IPAC2018)* (JACoW Publishing, Vancouver, BC, Canada, 2018), pp. 2872–2877.

[4] N. Samadi, B. Bassey, M. Martinson, G. Belev, L. Dallin, M. De Jong, and D. Chapman, A phase-space beam position monitor for synchrotron radiation, J. Synchrotron Radiat. **22**, 946 (2015).

[5] N. Samadi, X. Shi, L. Dallin, and D. Chapman, A real-time phase-space beam emittance monitoring system, J. Synchrotron Radiat. **26**, 1213 (2019).

[6] N. Samadi, X. Shi, L. Dallin, and D. Chapman, Source size measurement options for low-emittance light sources, Phys. Rev. Accel. Beams **23**, 024801 (2020).

[7] C. Thomas, G. Rehm, I. Martin, and R. Bartolini, X-ray pinhole camera resolution and emittance measurement, Phys. Rev. ST Accel. Beams **13**, 022805 (2010).

[8] C. A. Thomas and G. Rehm, Pinhole camera resolution and emittance measurement, in *Proceedings of the 11th*

European Particle Accelerator Conference, Genoa, 2008 (EPS-AG, Genoa, Italy, 2008), pp. 1254–1256.

[9] P. Elleaume, C. Fortgang, C. Penel, and E. Tarazona, Measuring beam sizes and ultra-small electron emittances using an x-ray pinhole camera, J. Synchrotron Radiat. **2**, 209 (1995).

[10] S. Marathe, X. Shi, M. J. Wojcik, N. G. Kujala, R. Divan, D. C. Mancini, A. T. Macrander, and L. Assoufid, Probing transverse coherence of x-ray beam with 2-D phase grating interferometer, Opt. Express **22**, 14041 (2014).

[11] X. Shi, S. Marathe, M. J. Wojcik, N. G. Kujala, A. T. Macrander, and L. Assoufid, Circular grating interferometer for mapping transverse coherence area of x-ray beams, Appl. Phys. Lett. **105**, 041116 (2014).

[12] T. W. Wysokinski, D. Chapman, G. Adams, M. Renier, P. Suortti, and W. Thomlinson, Beamlines of the Biomedical Imaging and Therapy Facility at the Canadian Light Source—Part 1, Nucl. Instrum. Methods Phys. Res., Sect. A **582**, 73 (2007).

[13] T. W. Wysokinski, D. Chapman, G. Adams, M. Renier, P. Suortti, and W. Thomlinson, Beamlines of the Biomedical Imaging and Therapy Facility at the Canadian Light Source —Part 2, *J. Phys. Conf. Ser.* 425, 072013 (2013).

[14] A. Koch, C. Raven, P. Spanne, and A. Snigirev, X-ray imaging with submicrometer resolution employing transparent luminescent screens, J. Opt. Soc. Am. A **15**, 1940 (1998).

[15] H. Onuki and P. Elleaume, *Undulators, Wigglers and Their Applications* (CRC Press, London, 2002).

[16] P. Cloetens, J. P. Guigay, C. De Martino, J. Baruchel, and M. Schlenker, Fractional Talbot imaging of phase gratings with hard x rays., Opt. Lett. **22**, 1059 (1997).

[17] J. P. Guigay, S. Zabler, P. Cloetens, C. David, R. Mokso, and M. Schlenker, The partial Talbot effect and its use in measuring the coherence of synchrotron x-rays., J. Synchrotron Radiat. **11**, 476 (2004).

[18] W. Grizolli, X. Shi, and L. Assoufid, Influence of optics vibration on synchrotron beam coherence, Opt. Lett. **44**, 899 (2019).

[19] J. W. Goodman, *Introduction to Fourier Optics* (McGraw-Hill, New York, 1996).

[20] J. C. Bergstrom and J. M. Vogt, The x-ray diagnostic beamline at the Canadian Light Source, Nucl. Instrum. Methods Phys. Res., Sect. A **587**, 441 (2008).

[21] N. Samadi, X. Shi, and D. Chapman, Optimization of a phase-space beam position and size monitor for low-emittance light sources, J. Synchrotron Radiat. **26**, 1863 (2019).

[22] Y. A. Babanov, A. V. Ryazhkin, A. F. Sidorenko, and L. A. Blaginina, Correcting an experimental absorption spectrum for the core level width, J. Struct. Chem. **39**, 833 (1998).

[23] S. Marathe, X. Shi, M. J. Wojcik, A. T. Macrander, and L. Assoufid, Measurement of x-ray beam coherence along multiple directions using 2-D checkerboard phase grating, J. Vis. Exp. **116**, e53025 (2016).

[24] N. Samadi, X. Shi, L. Dallin, and D. Chapman, Application of a phase space beam position and size monitor for synchrotron radiation source characterization, Phys. Rev. Accel. Beams **22**, 122802 (2019).